Structural and elastic behaviour of aragonite at high-pressure: a contribution from first-principle simulations

Gianfranco Ulian[1], Giovanni Valdrè[1,*]

1 Dipartimento di Scienze Biologiche, Geologiche e Ambientali, Centro di Ricerche Interdisciplinari di Biomineralogia, Cristallografia e Biomateriali, Università di Bologna "Alma Mater Studiorum" Piazza di Porta San Donato 1, 40126 Bologna, Italy.

Abstract

Aragonite ($CaCO_3$, space group *Pmcn*) is an important mineral for both geological and biological reasons, being one of the phases that recycles carbon in deep Earth conditions and the product of biomineralization of several terrestrial and marine organisms, respectively. Because of its ubiquity, aragonite has been the subject of several investigations to understand its elastic behaviour and stability at different *P-T* conditions, but the results reported in literature are still very scattered. Aiming at providing further details on this topic, in the present work we determined the structural and elastic properties of aragonite at absolute zero (0 K) within the Density Functional Theory framework, using *a posteriori* correction to include the weak long-range interactions. The equation of state parameters for this mineral phase, calculated between 0 GPa – 25 GPa, were K_0 = 80.2(7) GPa, K' = 4.37(10) and V_0 = 223.00(6) Å^3, in good agreement with the bulk modulus calculated from the elastic moduli (K_R = 78.49 GPa). The results were compared to previous experimental and theoretical data, finding them in line with some specific studies, and show that some structural features (e.g., the carbonate ion aplanarity) could be related to the mechanism of phase transition to the post-aragonite phase at high pressure. The present work highlights the importance of including van der Waals interactions in the physical treatment of the structural and elastic properties of aragonite, and further extends the knowledge of the behaviour of this mineral as a function of pressure.

Introduction

Aragonite $CaCO_3$ has drawn a lot of attention since the born of modern crystallography, as its structure has been determined by X-ray diffraction (XRD) first by Bragg (1924), then subsequent refinements followed (De Villiers, 1971; Santillán and Williams, 2004; Caspi et al., 2005; Antao and Hassan, 2009; Palaich et al., 2016). According to the cited studies, this mineral belongs to the orthorhombic class 2/*m* 2/*m* 2/*m*, space group *Pmcn* (sometimes also reported as *Pnma*, according to the crystal settings employed by the researchers), with four unit formulas in the crystallographic cell (Z = 4) and, at ambient conditions (1 atm, 298 K), a unit cell volume of about 227 Å^3 (De Villiers, 1971). According to De Villiers (1971), the cell parameters of aragonite are a = 4.9614(3) Å, b = 7.9671(4) Å and c = 5.7404(4) Å, which were confirmed by the recent results of Antao and Hassan (2009). An interesting feature of this mineral, related to its symmetry, is the slight non-planarity (also called aplanarity) of the CO_3^{2-} group and the two independent C–O distances. A structural model of orthorhombic aragonite is shown in Figure 1.

In addition to the crystallographic determinations, several efforts have been directed to investigate the elastic behaviour of aragonite at high pressure because of the importance of this mineral in both geological, biological and materials science fields. In fact, the calcium carbonate polymorphs aragonite (*Pmcn*) and calcite ($R\bar{3}$c) are the two most common forms of this compound that can be found on the surface of Earth, produced by both

biological and geological/physical processes (Palaich et al., 2016). While it is known that aragonite is a metastable polymorph at ambient conditions (Salje and Viswanathan, 1976), conversely it is the preferred structure synthesized by different organisms such as molluscs and corals (Farfan et al., 2021), and that participate in the formation of ocean floor deposits with other important minerals, for example, giving origin to clay-rich marls and carbonate ooze (Plank and Langmuir, 1998). Because of its high-pressure stability, aragonite is then the predominant form of calcium carbonate that contributes to deep-Earth recycling at subduction zones (Dasgupta and Hirschmann, 2010). To better understand the effects of high pressure and high temperature on the phase stability of this mineral, several experimental and theoretical researches focused their attention on both the hydrostatic compression behaviour (Martinez et al., 1996; Santillán and Williams, 2004; Ono et al., 2005; Oganov et al., 2006; Ono et al., 2007; Li et al., 2015; Wang et al., 2015; Palaich et al., 2016) and the uniaxial and biaxial elasticity (Voigt, 1910; Vizgirda and Ahrens, 1982; Pavese et al., 1992; Fisler et al., 2000; Liu et al., 2005; Huang et al., 2017).

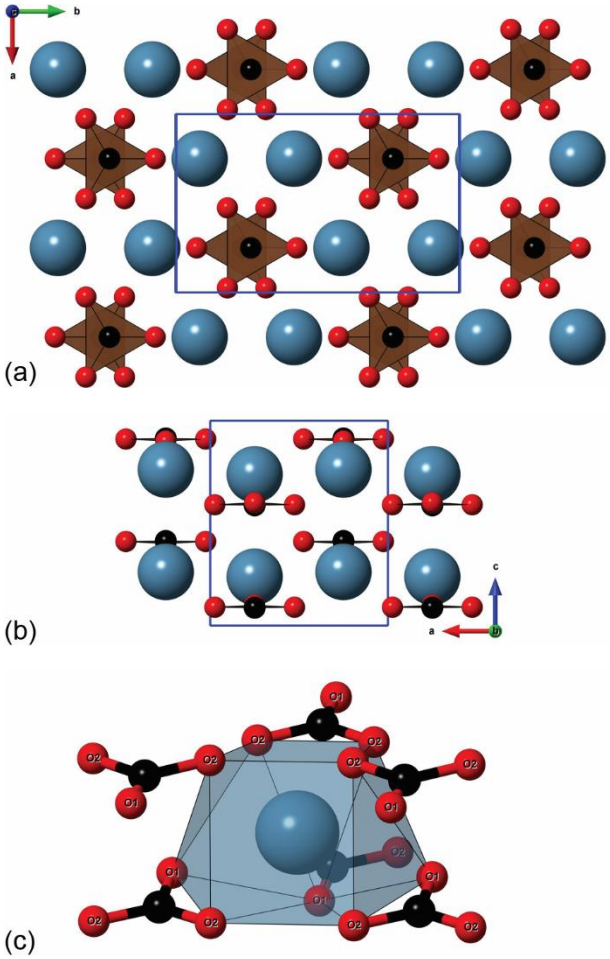

Figure 1. Aragonite structure as seen from (a) the [001] and (b) the [010] directions. The blue lines represent the unit cell of the mineral. (c) Polyhedral model of the 9-fold coordination of the Ca^{2+} ion with six carbonate groups, three O1 and six O2 oxygen atoms. Colour code for atoms: blue – Ca; red – O; black – C.

However, after a review on the subject, we noted that the results reported in literature were obtained with different methods and accuracies, related to specific experimental/theoretical approaches,

instrumental/computational setups, and sample purity. For example, the bulk modulus K_0 and its pressure derivative K' are scattered, with values in the ranges 64 – 88 GPa and 2.3 – 5.3, respectively. The same applies to the elastic moduli, *i.e.*, the components of the fourth-rank tensor physically/mathematically describing the stress-strain relationship (Nye, 1957), whose values show very high differences (as high as +1300%) between those of Voigt (1910) from ultrasonic scattering and the elastic moduli measured from Brillouin scattering by Liu and collaborators (2005).

In addition, from the theoretical perspective, no data were obtained so far including a proper treatment for long-range interactions. Albeit both aragonite and calcite are known to be an ionic solids, it was recently shown that long-range (dispersive) interactions play a key role in determining the structural, elastic and dielectric properties of calcite (Ulian et al., 2021a; Ulian et al., 2021b; Ulian and Valdrè, 2022b). We expect that dispersive forces will be then important for the description of the different mineralogical, physical, and chemical properties of aragonite as well, particularly its elastic behaviour.

For all the reasons cited above, in the present paper we investigated the structural and elastic behaviour of aragonite using first-principle simulations at the Density Functional Theory (DFT) level, including a proper treatment of long-range interactions. We calculated both the equation of state of the mineral under hydrostatic regime from 0 GPa up to 25 GPa, to analyse the effects of pressure on the structural features of the mineral, and the elastic moduli at zero pressure. A small expansion regime was included to better describe the compressional behaviour of aragonite. The considered pressure range encompasses a metastability region, as the phase transition from calcite to aragonite occurs at about 0.3 GPa at ambient temperature (Johannes and Puhan, 1971), and is below the experimentally observed phase transition from aragonite to post-aragonite, occurring at about 30 – 40 GPa (Ono et al., 2005; Ono et al., 2007). All the results were compared and discussed to data reported in literature.

Computational Methods

The simulations here presented were performed using the CRYSTAL17 *ab initio* code, which implements the Kohn–Sham self-consistent field (SCF) method (Dovesi et al., 2018). Throughout the present work, we employed the generalized-gradient approximation (GGA) exchange-correlation functional developed by Perdew-Burke-Ernzerhof, known as PBE (Perdew et al., 1996), and the hybrid functional B3LYP that, among the three-parameter exchange functional of Becke (1993) and the correlation term of Lee, Yang and Parr (1988), includes 20% of exact Hartree-Fock (HF) exchange. It is well-known that GGA functionals already provide adequate descriptions of the structural features of solid materials, but they are outperformed by hybrid functionals such as B3LYP for electronic (e.g., band structure), elastic and vibrational properties.

In CRYSTAL17, the construction of the multielectronic wave function is carried out using a linear combination of Gaussian-type functions (GTF), within the so-called linear combination of atomic orbitals (LCAO) approach. Calcium, carbon and oxygen were described in terms of 8-6511(21), 6-311(11) and 8-411(11) basis

sets, respectively, which were previously optimized by Valenzano and co-workers (2006). The chosen basis sets are well balanced, and was adopted for the investigation of both aragonite (Ungureanu et al., 2010; Carteret et al., 2013) and calcite (Ulian et al., 2021a; Ulian et al., 2021b; Ulian and Valdrè, 2022b), providing accurate results with sustainable computational costs.

The total energy was calculated on a pruned grid with 75 radial points and a maximum number of 974 angular points in regions relevant for chemical bonding, subdivided in five shells with different angular grids (Dovesi et al., 2018). The numerical accuracy for the calculation of the Coulomb and exchange integrals was set to 8 (ITOL1 to ITOL4) and 16 (ITOL5) (Dovesi et al., 2018). The Hamiltonian matrix was diagonalized on a 6×6×6 grid according to the Monkhorst-Pack (1976) scheme, which leads to 64 *k* points in the reciprocal space.

A well-known limitation of both GGA and hybrid Density Functional Theory functionals is the improper treatment of long-range interactions, which severely affects structural, vibrational, mechanical and other properties. The most common approach to overcome this issue is the *a posteriori* inclusion of an additional energy term to the DFT energy, which, in the present work, takes the form of the DFT-D2 and DFT-D3 formulations by Grimme and collaborators (Grimme, 2006; Grimme et al., 2010). The DFT-D2 contribution is described in the following formula:

$$E_{DFT-D2} = -\frac{1}{2}\sum_{i=1}^{N}\sum_{j=1}^{N}\sum_{\mathbf{g}}\frac{C_{6ij}}{r_{ij,\mathbf{g}}^{6}}\, f_{dump,6}\left(r_{ij,\mathbf{g}}\right)$$

The sums are over the atoms N in the unit cell, with $r_{ij,\mathbf{g}}$ the internuclear distance between atom i in cell $\mathbf{g} = 0$ (reference cell) and atom j in cell $\mathbf{g}$, and C_{6ij} the 6th-order dispersion coefficients for atom pairs ij. The long-range energy is damped by the function $f_{\mathrm{dump},6}(r_{\mathrm{ij},\mathbf{g}})$, to ensure that weak van der Waals interactions do not contribute to other ionic and covalent bonds, which exert their effects at short distances. The damping function is expresses as:

$$f_{dump,6}\left(r_{ij,\mathbf{g}}\right) = s_6\left[1 + e^{-d\left(r_{ij,\mathbf{g}}/R_{vdW}-1\right)}\right]^{-1}$$

with s_6 a scaling parameter that varies according to the adopted functional (e.g., for PBE it is 0.75), R_{vdW} the sum of van der Waals radii of atoms i and j and d the steepness of the damping, which was set to 20 in the present work, in agreement with the standard parametrization of the DFT-D2 approach (Grimme, 2006). The C_{6ij} parameters are calculated as a geometrical mean:

$$C_{6ij} = \sqrt{C_{6i}C_{6j}}$$

where C_{6i} and C_{6j} are tabulated for each atom and kept fixed during the simulation (Grimme, 2006). In the case of the B3LYP functional, the re-parametrization of Civalleri and collaborators (2008) of the terms in the equation reported above was employed, leading to the method named B3LYP-D*.

Within the DFT-D3 approach, the van der Waals contribution is given by (Grimme et al., 2010):

$$E_{DFT-D3} = -\frac{1}{2}\sum_{i=1}^{N}\sum_{j=1}^{N}\sum_{\mathbf{g}}\left[\frac{C_{6ij}}{r_{ij,\mathbf{g}}^{6}} f_{dump,6}\left(r_{ij,\mathbf{g}}\right) + \frac{C_{8ij}}{r_{ij,\mathbf{g}}^{8}} f_{dump,8}\left(r_{ij,\mathbf{g}}\right)\right]$$

where the C_{nij} (n = 6, 8) parameters are dependent on the geometry of the system, and not fixed as in the DFT-D2 scheme, hence the DFT-D3 correction is less empirical. The damping function here adopted is the one proposed by Becke and Johnson (Becke and Johnson, 2005; Johnson and Becke, 2005; Johnson and Becke, 2006):

$$f_{dump,n}\left(r_{ij,\mathbf{g}}\right) = \frac{s_n r_{ij}^{n}}{r_{ij}^{n} + f\left(R_{0ij}\right)^{n}}$$

with $R_{0ij} = \sqrt{C_{8ij}/C_{6ij}}$ and $f\left(R_{0ij}\right) = \alpha_1 R_{0ij} + \alpha_2$, $s_6 = 1$, s_8, whereas α_1 and α_2 are adjustable parameters. For a detailed explanation of the DFT-D*n* (n = 2, 3) corrections, the reader can refer to the works of Grimme and collaborators (Grimme, 2006; Grimme et al., 2010). In general, it is expected that the results from the DFT-D3 approach, which is less empirical than the DFT-D2 correction, would be in better agreement with the experimental ones.

The geometry optimization procedure of the structures consists in a simultaneous optimization of both the lattice constants with a numerical gradient method and the atomic internal coordinates using an analytical gradient approach. The Hessian matrix is upgraded with the Broyden–Fletcher–Goldfarb–Shanno algorithm (Broyden, 1970b; Broyden, 1970a; Fletcher, 1970; Goldfarb, 1970; Shanno, 1970). The tolerances for the maximum allowed gradient and the maximum atomic displacement for considering the geometry as converged have been set to $1 \cdot 10^{-5}$ hartree bohr^{-1} and $4 \cdot 10^{-5}$ bohr, respectively. This setup was adopted to find the equilibrium geometry at 0 GPa and the compressed/expanded states simulated to calculate the equation of state of the mineral, as also presented in previous works (Ulian et al., 2021a; Ulian et al., 2021b).

Second-order elastic moduli were calculated according to the scheme proposed by Perger and co-workers (2009), which is implemented in the CRYSTAL code. Very briefly, the elastic moduli are the components of the 4th-rank stiffness tensor **C**, which are defined as:

$$\sigma_{ij} = C_{ijkl}\varepsilon_{kl}$$

where σ_{ij} and ε_{kl} are the components of the stress and pure strain second-rank tensors, respectively, and the indeces *i*, *j*, *k*, *l* (= *x*, *y*, *z*) represents the Cartesian directions. A simpler notation is that proposed by Voigt, which replaces the $3 \times 3 \times 3 \times 3$ tensor with a 6×6 matrix whose elements are identified by the indices *v*,*u* = 1, …, 6, with 1 = *xx*, 2 = *yy*, 3 = *zz*, 4 = *yz*, 5 = *xz* and 6 = *xy* (Nye, 1957). This leads to the following expression:

$$\sigma_{v} = C_{vu}\varepsilon_{u}$$

The elements C_{vu} are also defined as the second derivative of the lattice energy with respect to the applied strain:

$$C_{vu} = \frac{\partial^2 E}{\partial \varepsilon_v \partial \varepsilon_u}\bigg|_0$$

where 0 indicates the stiffness is calculated at the equilibrium geometry. Aragonite is an orthorhombic mineral, which presents 9 independent elastic moduli and the stiffness matrix in Voigt notation is then:

$$\begin{pmatrix} C_{11} & C_{12} & C_{13} & \cdot & \cdot & \cdot \\ & C_{22} & C_{23} & \cdot & \cdot & \cdot \\ & & C_{33} & \cdot & \cdot & \cdot \\ & & & C_{44} & \cdot & \cdot \\ & & & & C_{55} & \cdot \\ & & & & & C_{66} \end{pmatrix}$$

where the small dots indicate elastic moduli having a value of zero. Six lattice deformations were needed to calculate the elastic moduli, namely

$$\varepsilon_1 = \delta \begin{pmatrix} 1 & 0 & 0 \\ 0 & 0 & 0 \\ 0 & 0 & 0 \end{pmatrix},\ \varepsilon_2 = \delta \begin{pmatrix} 0 & 0 & 0 \\ 0 & 1 & 0 \\ 0 & 0 & 0 \end{pmatrix},\ \varepsilon_3 = \delta \begin{pmatrix} 0 & 0 & 0 \\ 0 & 0 & 0 \\ 0 & 0 & 1 \end{pmatrix},$$

which represent the uniaxial strains, and

$$\varepsilon_4 = \delta \begin{pmatrix} 0 & 0 & 0 \\ 0 & 0 & 1 \\ 0 & 1 & 0 \end{pmatrix},\ \varepsilon_5 = \delta \begin{pmatrix} 0 & 0 & 1 \\ 0 & 0 & 0 \\ 1 & 0 & 0 \end{pmatrix},\ \varepsilon_6 = \delta \begin{pmatrix} 0 & 1 & 0 \\ 1 & 0 & 0 \\ 0 & 0 & 0 \end{pmatrix}$$

that are the biaxial (shear) stains. The factor δ controls the amount of applied strain, and in the present work it varied in the range ±0.015, with a step of 0.005, for a total of 7 configurations for each lattice strain. Single-crystal elastic properties, namely Young's modulus (E), linear compressibility (β), shear modulus (μ) and Poisson's ratio (υ) were calculated from the elastic moduli using the QUANTAS code (Ulian and Valdrè, 2022a), with well-known directional relations (Nye, 1957; Marmier et al., 2010; Gaillac et al., 2016; Ulian et al., 2018; Ulian and Valdrè, 2018b). Voigt and Reuss equations were employed to calculate the average elastic properties considering the system as a polycrystalline aggregate as explained by Nye (1957).

Graphical representations have been carried out with the molecular graphics program VESTA (Momma and Izumi, 2008).

Results and discussion

1. Crystal geometry

The results of the structural optimization in equilibrium conditions (absolute zero temperature and zero pressure), obtained from B3LYP-D*, B3LYP-D* and PBE-D2 approaches, compared to literature available

experimental ones, are reported in Table 1. The theoretical simulations produced data in very good agreement with previous experimental determinations of the crystal structure of aragonite (De Villiers, 1971; Caspi et al., 2005; Antao and Hassan, 2009). It is worth noting that experimental data were collected at room temperature (ca. 300 K), whereas no thermal contributions to the crystal structure (lattice vectors and atomic positions) was included in the present simulations.

Table 1. Equilibrium structure at 0 GPa of aragonite $CaCO_3$, with *V* the unit cell volume (Å^3), *a*, *b* and *c* the lattice parameters (Å), atomic distances (Å) and angles (°), aplanarity of the carbonate group (Å) and atomic fractional coordinates. Previous theoretical and experimental data are reported for a direct comparison.

		Theoretical				**Experimental**		
		B3LYP-D*[1]	B3LYP-D3[1]	PBE-D2[1]	B3LYP[2]	XRD[3]	XRD[4]	XRD[5]
V (Å^3)		229.535	222.987	228.968	235.666	226.906	227.011	227.081
a (Å)		5.0177	4.9544	5.0253	5.0080	4.9614	4.96062	4.96183
b (Å)		7.9005	7.8836	7.9358	8.0290	7.9671	7.97006	7.96914
c (Å)		5.7901	5.7091	5.7414	5.8610	5.7404	5.74181	5.74285
C–O1		1.2750	1.2756	1.2863	1.2789	1.279	1.281	1.2805
C–O2		1.2896	1.2865	1.2996	1.2891	1.284	1.284	1.2931
mean C–O		1.2847	1.2829	1.2952	1.2857	1.282	1.283	1.289
Ca–O1 (×1)		2.4266	2.4054	2.4122	2.4324	2.419	2.403	2.4127
Ca–O1 (×2)		2.6953	2.6488	2.6929	-	2.653	2.6521	2.6570
Ca–O2 (×2)		2.4550	2.4342	2.4394	-	2.445	2.473	2.4438
Ca–O2 (×2)		2.5184	2.4973	2.5231	-	2.520	2.494	2.5197
Ca–O2 (×2)		2.5491	2.5278	2.5576	-	2.550	2.558	2.5457
mean Ca–O		2.5402	2.5135	2.5376	-	2.528	2.5286	2.5272
O1–C–O2		120.44	120.36	120.42	-	120.19	119.2	120.15
O2–C–O2		118.98	119.12	118.97	-	119.55	120.8	119.38
mean O–C–O		119.95	119.95	119.94	-	119.98	119.73	119.89
aplanarity		0.0274	0.0297	0.0326	-	0.0193	0.0291	0.0420
Ca (4*c*)								
	x/a	1/4	1/4	1/4	1/4	1/4	1/4	1/4
	y/b	0.41376	0.41508	0.41425	0.41553	0.4150	0.4150	0.4150
	z/c	0.76364	0.76164	0.76318	0.75970	0.7597	0.7577	0.7599
C (4*c*)								
	x/a	1/4	1/4	1/4	1/4	1/4	1/4	1/4
	y/b	0.76542	0.76448	0.76562	0.76222	0.7622	0.7616	0.7619
	z/c	–0.08445	-0.08618	–0.08308	–0.08144	–0.0862	–0.0808	–0.0824
O1 (4*c*)								
	x/a	1/4	1/4	1/4	1/4	1/4	1/4	1/4
	y/b	0.92664	0.92606	0.92746	0.92138	0.9225	0.9220	0.9224
	z/c	–0.09443	-0.09807	–0.09549	–0.09008	–0.0962	–0.0944	–0.0945
O2 (8*d*)								
	x/a	0.47143	0.47388	0.47279	0.47219	0.4736	0.4750	0.4750
	y/b	0.68257	0.62182	0.68248	0.68118	0.6810	0.6824	0.6801
	z/c	–0.08648	-0.08795	–0.08532	–0.08435	–0.0862	–0.0905	–0.0873

Notes: Wyckoff sites are reported in parentheses after each atom.
1 – present work; 2 – simulations results of Carteret and co-workers (2013); 3 – X-ray diffraction results reported by De Villiers (1971); 4 – X-ray diffraction results reported by Antao and Hassan (2009); 5 – High-resolution synchrotron powder diffraction measurements of Caspi et al. (2005)

In details, the unit cell volume calculated with both the B3LYP-D* and PBE-D2 approaches is within about 1% of deviation with respect to the XRD refinements. This overall effect is due to an interplay of increased *a*

(about +1.2%) and *c* (+0.9%) lattice parameters and a shrinking of the **b**-axis length (between –0.4% and –0.8%), whose extents depend on the adopted DFT functional. The **a**-axis value seems related to the C–O2 bond distance, which is systematically larger in our simulations (+0.4% and +1.2% at B3LYP-D* and PBE-D2 levels, respectively) than in the X-ray diffraction experiments. The use of the less empirical treatment of the van der Waals interactions (*i.e.*, the DFT-D3 approach) resulted in a unit cell volume that is smaller than the experimental ones by about 1.7%, with all the lattice vectors shorter than those from the XRD refinements. In general, these observations are in line with the analysis of the effects of the inclusion of long-range interactions, where the same functionals and corrections were adopted to investigate calcite (Ulian et al., 2021a). However, it should be noted that a smaller unit cell is what should be expected in static DFT simulations, which do not include any temperature effect (*e.g.*, thermal expansion), because XRD measurements are typically performed at $T > 0$ K. The reason behind this small discrepancy probably resides in the long-range interactions, as the sole B3LYP produced a unit cell with increased volume of about +4% (Carteret et al., 2013), the B3LYP-D* and PBE-D2 approaches partially amend it, and the B3LYP-D3 combination produced the expected results.

The aplanarity of the carbonate ion, *i.e.*, the distance between the C atom from the plane described by the three oxygen atoms from our simulations is within the values measured by XRD crystallographic data (0.0193 Å – 0.0420 Å).

Considering the previous structure determination obtained with the CRYSTAL code by Carteret and co-workers (2013), the unit cell calculated at the B3LYP level without including the effects of van der Waals interactions (see Table 1) is larger than ours obtained with the B3LYP-D* and B3LYP-D3 approach by about +2.5% and 5.4%, respectively, and deviating by about +4% from the XRD data. The difference in the computational settings between the present work and the one of Carteret et al. (2013) resides only on the presence of the DFT-D*n* correction, further confirming that van der Waals interactions are important also for ionic minerals/materials as aragonite and calcite (Ulian et al., 2021a). Furthermore, our structural results are also in better agreement with the experiments than those reported by Huang et al. (2017), who obtained a = 5.002 Å, b = 8.014 Å and c = 5.792 Å by employing pseudopotentials plane-wave basis sets and the PBE functional (with no correction for van der Waals interactions).

2. Equation of state

To calculate the equation of state of aragonite, a set of larger (expansion) and smaller (compression) unit cells were geometrically optimized at fixed volume. This is a well-known approach for simulating how the unit cell volume varies with hydrostatic pressure [see for instance (Ottonello et al., 2010; Ungureanu et al., 2010; Ulian and Valdrè, 2017; Ulian and Valdrè, 2018a)]. Thirteen unit cell volumes between 85% and 106% of the equilibrium unit cell volume, V_{eq}, were modelled according to the EOS routine implemented in CRYSTAL (Erba et al., 2014). The equation of state was then calculated from the $E(V)$ data, *i.e.*, energy versus volume curves, employing the volume-integrated 3rd-order Birch-Murnaghan (BM3) formulation (Birch, 1947), as proposed by Hebbache and Zemzemi (2004):

$$E(V) = E_0 + \frac{9}{16} K_0 V_0 \left\{ K' \left(X^2 - 1 \right)^3 + \left[\left(X^2 - 1 \right)^2 \left(6 - 4X^2 \right) \right] \right\}$$

In this equation, the fitting parameters are E_0, K_0, K' V_0, which represent the unit cell energy, the bulk modulus and its pressure first derivative, and the unit cell volume V_0, respectively. The term $X = (V_0/V)^{-1/3}$ was introduced to ease the readability of the formula, and the subscript zero in the different parameters means that the values are related to a zero-pressure (0 GPa) condition. The structural data of aragonite at different compression states are reported in Tables 2, 3 and 4 for the simulations performed with B3LYP-D*, B3LYP-D3 and PBE-D2, respectively.

Table 2. Unit cell volume, lattice parameters, mean bond lengths and angles and CO_3^{2-} aplanarity as a function of pressure, as obtained from DFT/B3LYP-D* simulations.

P (GPa)	*V* (Å^3)	*a* (Å)	*b* (Å)	*c* (Å)	<C–O> (Å)	<Ca–O> (Å)	<O–C–O> (°)	aplanarity (Å)
24.4	186.076	4.7897	7.4681	5.2020	1.2698	2.3718	119.94	0.0316
20.3	190.752	4.8248	7.4777	5.2872	1.2718	2.3910	119.94	0.0316
15.2	197.473	4.8619	7.5430	5.3847	1.2746	2.4177	119.94	0.0309
13.2	200.508	4.8793	7.5702	5.4283	1.2758	2.4275	119.94	0.0306
11.2	203.839	4.8972	7.6021	5.4753	1.2770	2.4428	119.94	0.0302
9.2	207.386	4.9157	7.6402	5.5219	1.2783	2.4566	119.95	0.0298
7.2	211.312	4.9346	7.6868	5.5709	1.2796	2.4717	119.95	0.0293
5.2	215.719	4.9553	7.7381	5.6258	1.2809	2.4885	119.95	0.0288
3.1	220.709	4.9775	7.7985	5.6859	1.2825	2.5073	119.95	0.0283
1.1	226.392	5.0036	7.8636	5.7538	1.2839	2.5286	119.95	0.0277
0.1	229.535	5.0177	7.9005	5.7901	1.2847	2.5402	119.95	0.0274
-1.0	232.979	5.0325	7.9407	5.8301	1.2856	2.5527	119.49	0.0271
-2.0	236.772	5.0495	7.9834	5.8735	1.2865	2.5679	119.53	0.0269
-3.1	240.983	5.0682	8.0315	5.9202	1.2873	2.5849	119.56	0.0266

Table 3. Unit cell volume, lattice parameters, mean bond lengths and angles and CO_3^{2-} aplanarity as a function of pressure, as obtained from DFT/B3LYP-D3 simulations.

P (GPa)	*V* (Å^3)	*a* (Å)	*b* (Å)	*c* (Å)	<C–O> (Å)	<Ca–O> (Å)	<O–C–O> (°)	aplanarity (Å)
24.9	183.326	4.7411	7.5353	5.1315	1.2685	2.3587	119.93	0.0333
20.6	187.733	4.7711	7.5537	5.2092	1.2705	2.3764	119.93	0.0332
15.4	194.010	4.8104	7.5914	5.3127	1.2732	2.4015	119.93	0.0328
13.3	196.876	4.8265	7.6145	5.3571	1.2744	2.4128	119.93	0.0327
11.2	199.921	4.8426	7.6425	5.4019	1.2756	2.4248	119.94	0.0324
9.2	203.248	4.8601	7.6725	5.4506	1.2768	2.4378	119.94	0.0320
7.1	206.844	4.8786	7.7081	5.5005	1.2780	2.4518	119.94	0.0316
5.1	210.820	4.8977	7.7517	5.5530	1.2793	2.4672	119.94	0.0310
3.1	215.251	4.9184	7.8004	5.6105	1.2807	2.4842	119.94	0.0305
1.0	220.256	4.9415	7.8542	5.6750	1.2821	2.5032	119.95	0.0300
0.0	222.987	4.9544	7.8836	5.7091	1.2829	2.5135	119.95	0.0297
-1.0	225.925	4.9681	7.9150	5.7455	1.2837	2.5293	119.56	0.0294
-2.0	229.111	4.9822	7.9490	5.7851	1.2844	2.5419	119.58	0.0291
-3.1	232.563	4.9981	7.9866	5.8260	1.2852	2.5558	119.60	0.0288

The BM3 fitted parameters were K_0 = 69.10(7) GPa, K' = 4.73(1) and V_0 = 229.174(6) Å^3 by considering the PBE-D2 results, K_0 = 71.7(8) GPa, K' = 4.18(11) and V_0 = 229.77(8) Å^3 with B3LYP-D* and K_0 = 80.2(7)

GPa, K' = 4.37(10) and V_0 = 223.00(6) Å^3 at B3LYP-D3 level. Generally, GGA functionals such as PBE are affected by underbinding, namely bond distances are typically larger and the bulk moduli lower than those experimentally measured. However, this effect is reduced by correcting the PBE total energy with the D2 scheme (*i.e.*, cancellation of errors), providing structural and elastic data that are more in line with experimental samples. For example, Huang et al. (2017) performed theoretical simulations at the DFT/PBE level of theory without the inclusion of van der Waals interactions and reported third-order Birch-Murnaghan parameters K_0 = 66.09 GPa, K' = 4.64 and V_0 = 232.5 Å^3. These values are in line with ours but show a larger unit cell volume at zero pressure. It is interesting noting that our results obtained with two Hamiltonians are very close to each other, but with a slightly different value of the K' term. In fact, the simulations carried out with the hybrid DFT functional and the DFT-D2 scheme led to a first derivative of the bulk modulus $K' \approx 4$, conversely $K' > 4$ by using the PBE-D2 and B3LYP-D3 approaches. Generally, when the first derivative of the bulk modulus is close to 4, the elastic behaviour under hydrostatic compression is described as a second-order Birch-Murnaghan, whereas $K' \neq 4$ suggests that the BM3 formulation is better suited for the description of the pressure evolution of a solid phase. However, the results from the different approaches fall within the experimental findings, with very small differences between each other. The bulk modulus values are also expected being in general larger than the experimental ones, because they are referred to aragonite at absolute zero (0 K).

Table 4. Unit cell volume, lattice parameters, mean bond lengths and angles and CO_3^{2-} aplanarity as a function of pressure, as obtained from DFT/PBE-D2 simulations.

P (GPa)	V (Å^3)	a (Å)	b (Å)	c (Å)	<C–O> (Å)	<Ca–O> (Å)	<O–C–O> (°)	aplanarity (Å)
23.4	187.317	4.8074	7.5241	5.1785	1.2809	2.3769	119.92	0.0367
19.6	191.507	4.8364	7.5310	5.2579	1.2828	2.3936	119.92	0.0373
16.4	195.511	4.8625	7.5572	5.3204	1.2845	2.4098	119.92	0.0372
13.5	199.540	4.8862	7.5925	5.3786	1.2862	2.4257	119.92	0.0369
11.0	203.619	4.9084	7.6336	5.4344	1.2877	2.4415	119.92	0.0365
8.6	207.744	4.9296	7.6789	5.4881	1.2891	2.4576	119.92	0.0359
6.5	211.930	4.9500	7.7280	5.5401	1.2905	2.4737	119.93	0.0353
4.7	216.162	4.9694	7.7802	5.5909	1.2918	2.4898	119.93	0.0346
2.9	220.450	4.9882	7.8338	5.6415	1.2930	2.5059	119.93	0.0339
1.4	224.791	5.0069	7.8870	5.6925	1.2942	2.5221	119.93	0.0332
0.1	228.968	5.0253	7.9358	5.7414	1.2952	2.5376	119.94	0.0326
-1.3	233.633	5.0441	7.9937	5.7943	1.2963	2.5547	119.94	0.0320
-2.4	238.135	5.0619	8.0492	5.8446	1.2973	2.5711	119.94	0.0314
-3.5	242.689	5.0793	8.1056	5.8948	1.2982	2.5875	119.94	0.0309

Compared to experimental findings (see Table 5), our BM3 equation of state parameters are in good agreement with all the results obtained with the same formulation (Ono et al., 2005; Li et al., 2015) and with a second-order Birch-Murnaghan equation of state, as proposed by Martinez et al. (1996). As expected, because no temperature effects were included in the simulations, the bulk moduli are generally higher than the experimental ones, in the order PBE-D2 < B3LYP-D* < B3LYP-D3. A much higher bulk modulus (K_0 = 88 GPa) was obtained by Santillán and Williams (2004), because of a large differential stress induced in the sample chamber as the pressure increased. According to previous discussions and comments (Ono et al., 2005;

Palaich et al., 2016), this effect could be explained by the freezing of the methanol-ethanol mixture used as pressure-transmitting medium above 10 GPa, which led to a non-hydrostatic behaviour during the experiments and to a significant strain-broadening of the XRD diffraction peaks. Our simulations at 0 K, since they represent the higher bound of the bulk modulus of aragonite, seems supporting this discussion.

More details can be graphically evinced from Figure 2, which reports the evolution of the unit cell volume and lattice parameters as a function of pressure. It can be noted that our theoretical results are in very good agreement with most of the experimental data (Martinez et al., 1996; Palaich et al., 2016; Litasov et al., 2017), with a small systematic overestimation of the *a* lattice parameter. As discussed for aragonite at equilibrium conditions, this is probably due to missing long-range interactions along the **a-**axis direction, which are better described with the combination of the DFT-D3 correction and the B3LYP functional. In general, the trend is not linear in the explored pressure range for each lattice vector, especially for the **b**-axis that shows an almost parabolic behaviour. Such peculiar trend was observed by Palaich and co-workers (2016), and it was explained as a stiffening of the **b**-axis of aragonite above about 15 GPa, being the dependence of the lattice parameter with pressure flatten above this pressure threshold. Because of the loss of hydrostatic/elastic regime, the data of Santillán and Williams (2004) show high discrepancy above 15 GPa.

Table 5. Comparison between the *P*-*V* equation of state parameters of aragonite obtained in different studies.

K_0 (GPa)	K'	V_0 (Å^3)	Method	Formulation	Reference
64.81(3.48)	4*	227.5(8)	MA	BM2	Martinez et al. (1996)
88(3)	4*	226.7(3)	DAC	BM2	Santillán and Williams (2004)
67.1(6.3)	4.7(8)	227.2(1.0)	DAC	BM3	Ono et al. (2005)
73.1(2.2)	4*	-	DAC	BM2	Ono et al. (2005)
65.24(24)	4.95(12)	226.72(1)	DAC	BM3	Li et al. (2015)
66.5(7)	5.0(1)	226.932(5)*	DAC	BM3	Palaich et al. (2016)
65.7(8)	5.1(1)	227.11(3)*	MA	VR	Litasov et al. (2017)
67.0(8)	4.74(12)	227.11(3)*	MA	BM3	Litasov et al. (2017)
66.09	4.64	232.5	DFT/PBE	BM3	Huang et al. (2017)
69.10(7)	4.73(1)	229.174(6)	DFT/PBE-D2	BM3	Present work
71.7(8)	4.18(11)	229.77(8)	DFT/B3LYP-D*	BM3	Present work
80.2(7)	4.37(10)	223.00(6)	DFT/B3LYP-D3	BM3	Present work

Notes: values with an asterisk (*) were kept fixed during the fitting procedure. MA = multianvil, DAC = diamond-anvil cell. Formulations are 2nd-order Birch-Murnaghan (BM2), 3rd-order Birch-Murnaghan (BM3) and Vinet-Rydberg (VR).

Regarding the internal geometry (see Figure 3), we found that the different Ca – O and C – O bond lengths show a continuous decrease by increasing pressure. In particular, the Ca – O bonds show the highest decrease in distance at the maximum investigated pressure (mean Ca – O length ≈ 6.3%, ≈ 6.5% and 6.2% with PBE-D2, B3LYP-D* and B3LYP-D3, respectively), whereas the C – O bonds shortened by about 1.1% (Figures 3a, b). This is in good agreement with both the experimental observation of Antao and Hassan (2009) and the theoretical simulations of Li and collaborators (2015), who also assessed the rigid behaviour of the carbonate ion. In addition, there is an anisotropic variation of the specific Ca – O distances, with the Ca – O1 bonds on the *ab* plane showing less shrinking (≈6.3% at PBE-D2 and about 6.5% with B3LYP-D*) than the Ca – O2 bonds on the same crystallographic plane (about 6.8% and 7.1% with PBE-D2 and B3LYP-D*, respectively). At B3LYP-D3 level the two bonds show a similar shrinking of about 6.3%.

However, the present simulation results seem not to confirm the experimental observation of Palaich and collaborators (2016). According to the cited research, at ambient pressure, the carbonate groups have their oxygen atoms positioned to form equilateral triangles, with both bond angles equal to 120°, whereas they become isosceles triangles by increasing pressure. At ca. 29 GPa, the authors noted a difference between the O1 – C – O2 and O2 – C – O2 angles of about 10°. Albeit we did not reach this pressure condition, the difference within the same bond angle is about 0.5° between 0 GPa and 25 GPa, with a divergence of 2–3° between the two bond angles at the maximum investigated pressure (Figure 3c). In addition, due to symmetry reasons, in our simulations the triangles described by the oxygens of CO_3^{2-} groups are always isosceles.

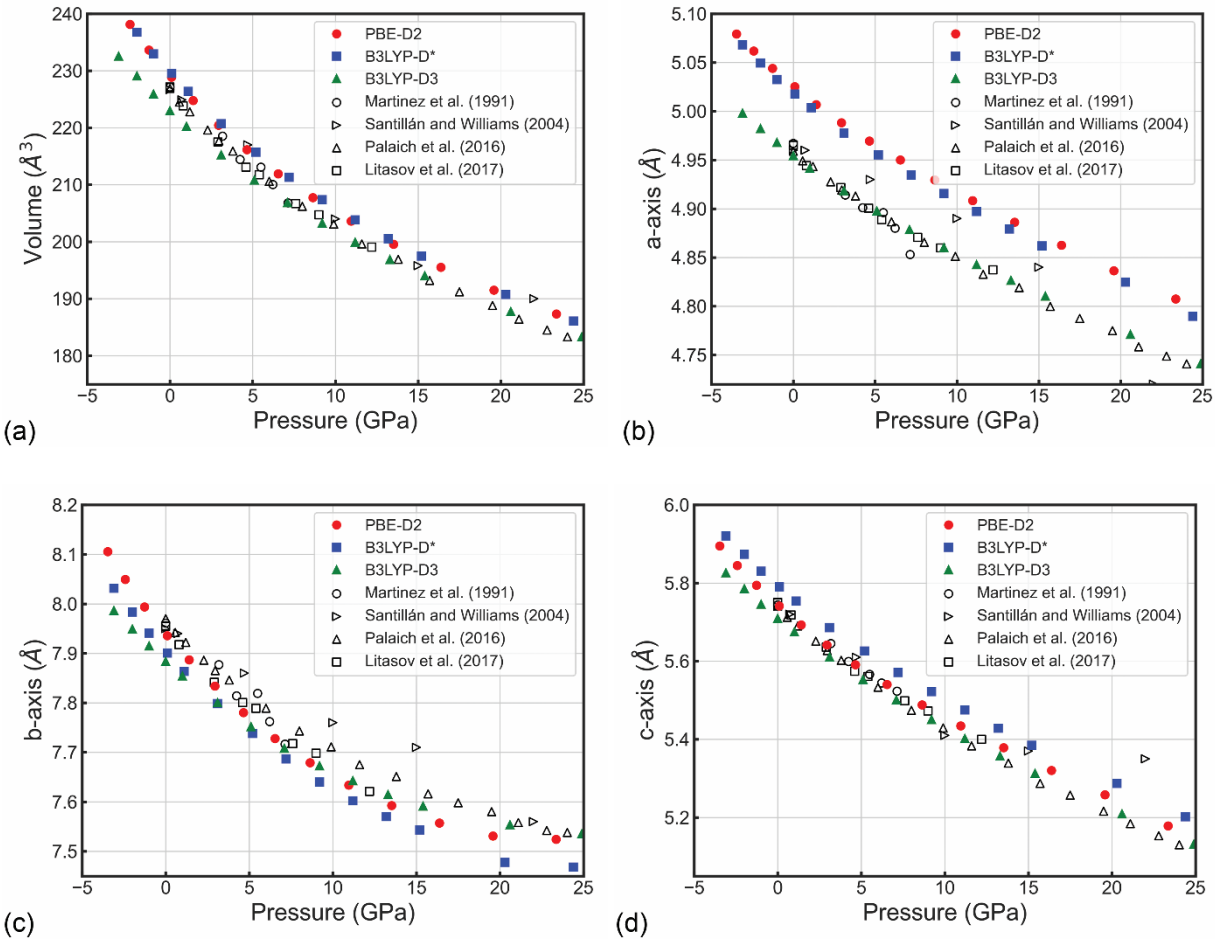

Figure 2. Aragonite (a) unit-cell volume, (b) **a**-axis, (c) **b**-axis and (d) **c**-axis as a function of pressure, as obtained from Density Functional Theory simulations at the PBE-D2, B3LYP-D* and B3LYP-D3 levels. Results from previous experimental findings are reported for a direct comparison.

Finally, it is interesting to note that the aplanarity of the carbonate ion group increases as a function of pressure (Figure 3d), with an almost linear trend up to about 15 GPa for the B3LYP functional with both DFT-D*n* corrections for long-range interactions. Instead, a maximum value was found for the PBE-D2 functional at about 20 GPa, then aplanarity starts decreasing by further compressing the mineral. Conversely, at the B3LYP level it was observed a flattening in the aplanarity to about 0.0316 Å and 0.0333 Å with DFT-D2 and DFT-D3 schemes, respectively. This incipient discontinuity could be a sign of initial crystal-structural changes related

to the aragonite to post-aragonite phase transition. However, to fully support this statement it would be required the theoretical analysis of the post-aragonite structure (space group *Pmmn*), which is beyond the scope of this work.

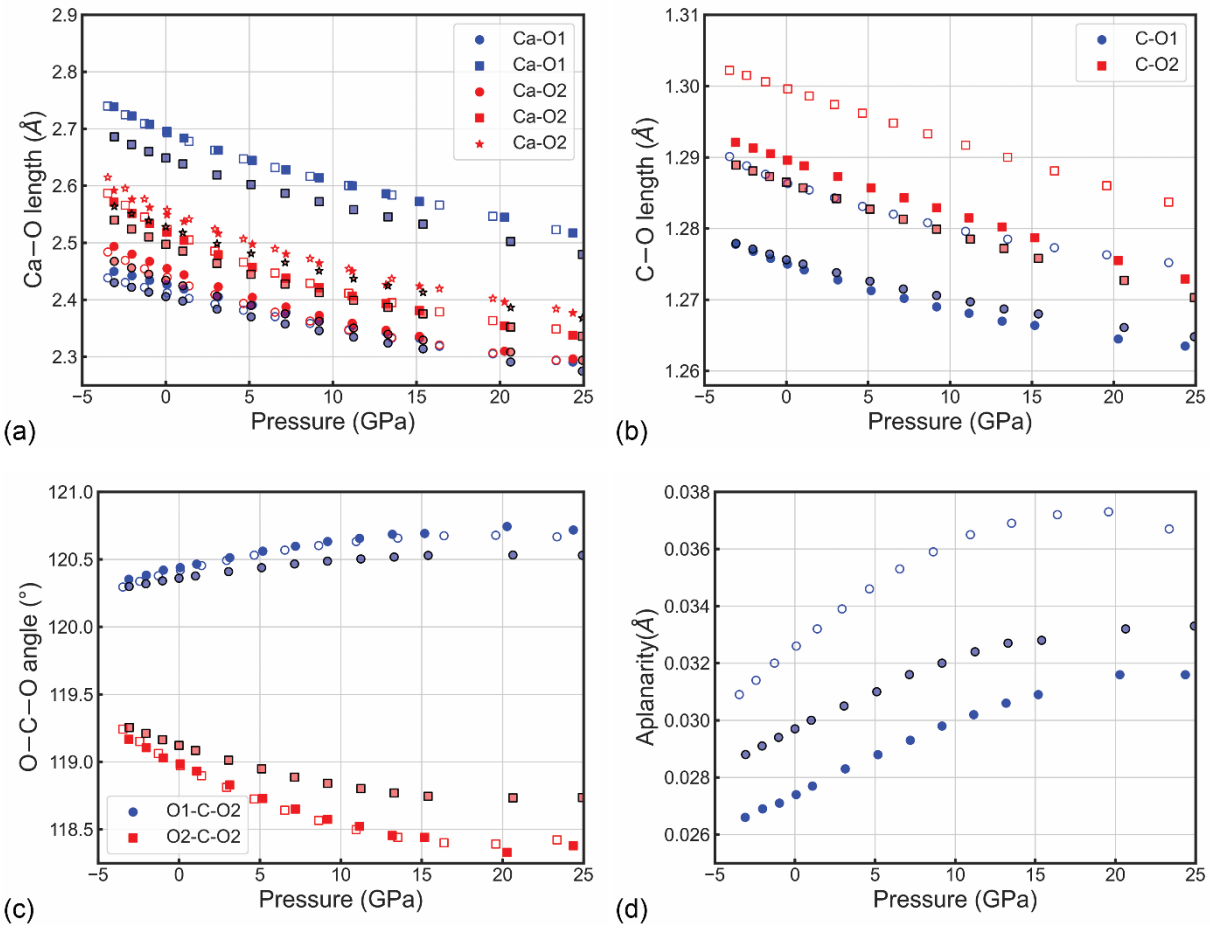

Figure 3. (a) Ca – O and (b) C – O bond distances, (c) O – C – O bond angles and (d) aplanarity of the carbonate group in aragonite as a function of pressure. Open and filled symbols are related to PBE-D2 and B3LYP-D* results, respectively, whereas the B3LYP-D3 values are shown with coloured symbols with black edges.

3. Elastic moduli

Table 6 reports the elastic moduli of aragonite calculated with the proposed PBE-D2, B3LYP-D* and B3LYP-D3 approaches at 0 K and 0 GPa. The mineral is mechanically stable in these conditions, according to the Born criteria depicted by Mouhat and Coudert (2014):

$$C_{11} > 0$$
$$C_{11}C_{22} > C_{12}^2$$
$$C_{11}C_{22}C_{33} + 2C_{12}C_{13}C_{23} - C_{11}C_{23}^2 - C_{22}C_{13}^2 - C_{33}C_{12}^2 > 0$$
$$C_{44} > 0$$
$$C_{55} > 0$$
$$C_{66} > 0$$

Typically, the Reuss bulk modulus K_R obtained from the elastic moduli of a crystal should be close to the K_0 parameter obtained from the equation of state. Our simulations respect this condition, as the difference between the two values are below 0.1%.

Table 6. Elastic moduli C_{ij} (GPa), bulk modulus (K, GPa), axial compressibility (β_x, TPa^{-1}), Young's modulus (E, GPa), shear modulus (μ, GPa) and Poisson's ratio (υ) of aragonite, obtained from both theoretical and experimental means.

	Theoretical						**Experimental**	
	B3LYP-D3	B3LYP-D*[1]	PBE-D2[1]	SM[2]	RIM1[3]	PBE[4]	BS[5]	US[6]
C_{11}	195.31	168.35	178.10	155.3	164.4	162.57	171.1	159.6
C_{22}	121.11	106.50	104.58	104.2	112.0	107.81	110.1	87.0
C_{33}	114.34	106.33	104.31	89.9	59.2	96.48	98.4	85.0
C_{44}	46.96	41.31	39.74	36.7	40.5	41.91	39.3	41.3
C_{55}	27.95	19.60	24.33	12.4	33.9	36.44	24.2	25.6
C_{66}	43.54	38.29	37.92	23.3	49.0	19.59	40.2	42.7
C_{12}	71.34	65.68	63.11	55.9	65.3	53.65	60.3	36.6
C_{13}	32.99	27.32	28.85	54.7	39.0	26.42	27.8	2.0
C_{23}	52.96	44.35	44.76	48.0	48.2	42.77	41.9	15.9
K_V	83.04	72.88	73.38	74.1	80.3	67.6	71.1	49.0
K_R	78.49	69.37	69.16	69.6	76.5	64.3	66.7	44.7
K_{VRH}	80.76	71.12	71.27	71.8	78.4	66.0	68.9	46.8
β_a	2.6	3.0	2.7	2.1	2.1	3.5	3.0	4.3
β_b	3.9	4.8	5.1	5.2	1.6	4.6	4.6	7.8
β_c	6.2	6.6	6.7	7.1	14.2	7.4	7.3	10.2
E_V	107.94	92.94	95.21	72.7	88.5	91.7	95.4	95.0
E_R	98.60	82.03	86.53	61.7	81.3	81.6	87.6	86.3
E_{VRH}	103.27	87.50	90.88	67.2	84.9	86.7	91.5	90.7
μ_V	42.05	36.09	37.08	27.2	33.6	36.0	37.4	40.4
μ_R	38.20	31.48	33.50	22.8	30.7	31.7	34.2	36.6
μ_{VRH}	40.13	33.79	35.29	25.0	32.2	33.8	35.8	38.5
υ_V	0.283	0.287	0.284	0.336	0.316	0.274	0.276	0.176
υ_R	0.291	0.303	0.291	0.352	0.323	0.289	0.281	0.178
υ_{VRH}	0.287	0.295	0.287	0.344	0.320	0.281	0.279	0.177

Notes: subscripts V, R and VRH indicate the Voigt, Reuss and Hill averaging schemes, respectively.
1 – present work
2 – shell model (SM) simulation results of Fisler et al. (2000)
3 – simulations carried out using rigid ion model (RIM) by Pavese and co-workers (1992)
4 – *ab initio* simulations of Huang and collaborators (2017)
5 – Brillouin spectroscopy (BS) results of Liu et al. (2005)
6 – ultrasonic scattering (US) measurements (Voigt, 1910)

The calculated elasticity of the mineral is in general good agreement with the Brillouin scattering measurements at ambient conditions (1 atm, 298 K) made by Liu and co-workers (2005), with mean absolute deviations of about 16.3% for B3LYP-D3, 6.5% for B3LYP-D* and 4.2% for PBE-D2. Part of this variation is related to the use of localized basis sets, as discussed by the authors in previous literature (Ulian and Valdrè, 2018b; Ulian et al., 2021b). The slightly better agreement of PBE is due to a cancellation of errors effect, *i.e.*, the pure GGA functional typically underestimates the bulk modulus of materials, which cancels out part of the

overestimation of the elastic moduli introduced by the GTO basis sets. However, as previously mentioned when discussing the crystal-chemistry and the equation of state, a higher and positive difference between the theoretical and experimental elastic moduli is expected. In fact, both the PBE-D2 and the B3LYP-D* method provided a mix of underestimated and overestimated C_{ij} terms. From this perspective, the results from the GTO/B3LYP-D3 approach are more representative of the behaviour of aragonite at 0 K and without any thermal and zero-point effects, because the elastic moduli are systematically larger than the experimental ones.

We observe the trend in the longitudinal elastic moduli (*i.e.*, C_{ii}, with i = 1, 2, 3) $C_{11} > C_{22} > C_{33}$, in agreement with both experimental (Liu et al., 2005) and theoretical findings (Pavese et al., 1992; Fisler et al., 2000; Huang et al., 2017). It is interesting to note that our simulations provided $C_{22} \approx C_{33}$ with PBE-D2 and B3LYP-D* DFT Hamiltonians, a result that is in line with the ultrasonic measurements of Voigt (1910). However, the present results confirm previous theoretical and experimental evidences of the larger values of the off-diagonal elastic moduli (C_{12}, C_{13}, and C_{23}) compared to the very old values reported by Voigt (1910). An improvement with respect to previous simulations is the calculated value of the C_{13} elastic moduli (27.32 GPa and 28.85 GPa at B3LYP-D* and PBE-D2 levels, respectively), which is in very good agreement with the experimental value of Liu and co-workers (2005).

The linear axial compressibilities, β_x, with $x = a$, b and c, were calculated for an orthorhombic crystal as explained by Nye (1957) using the formula:

$$\beta_a = \frac{d\left(a/a_0\right)}{dP} = s_{11} + s_{12} + s_{13}$$

$$\beta_b = \frac{d\left(b/b_0\right)}{dP} = s_{12} + s_{22} + s_{23}$$

$$\beta_c = \frac{d\left(c/c_0\right)}{dP} = s_{13} + s_{23} + s_{33}$$

where s_{ij} are the elements of the compliance tensor $S = C^{-1}$, expressed in Voigt's notation. For an orthorhombic mineral the volume compressibility $\beta = K^{-1}$ is linked to the axial compressibilities according to the following expression:

$$\beta = \beta_a + \beta_b + \beta_c$$

Our DFT axial compressibility values are reported in Table 6, and they are in very good agreement with the experimental data of Liu et al. (2005), and provide an improvement with respect to classical potential models (Pavese et al., 1992; Fisler et al., 2000) and standard first-principle GGA approaches (Huang et al., 2017).
The wave velocities were calculated for single-crystal aragonite according to the Christoffel's equation, as reported by Musgrave (1970):

$$\left|C_{ijkl}\eta_j\eta_l - \rho V^2\delta_{ik}\right| = 0$$

where C_{ijkl} are the elastic moduli, η is the propagation direction, ρ is the mineral density, V is the wave velocity and δ_{ik} is the Kronecker's delta function. The primary (P-wave, longitudinal, V_P) and secondary (S-wave, transverse, V_S) acoustic wave velocities of aragonite were calculated using the MTEX software (Mainprice et al., 2011), and the results are graphically reported in Figure 4.

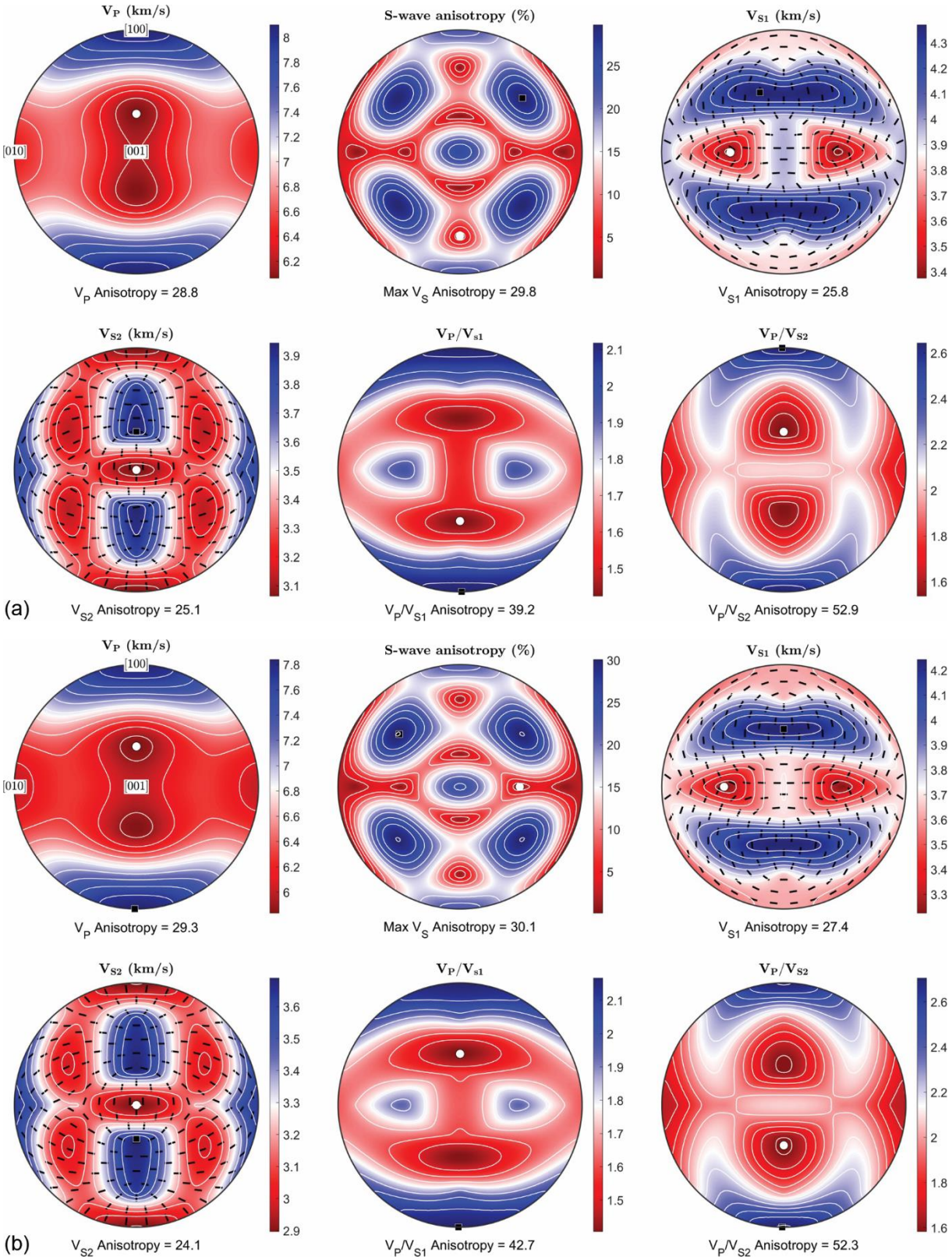

Figure 4. Analysis of the seismic wave velocities (Lambert equal-area upper hemisphere projections), showing (from upper left to lower right panels) the longitudinal wave velocity V_P (km/s), the anisotropy of secondary waves (%), the fast and slow secondary wave velocities, V_{S1} and V_{S2}, respectively (km/s), both with polarization directions, the V_P/V_{S1} and V_P/V_{S2} velocity ratios. Under each projection, the corresponding anisotropy value is reported (see text for details). The black and white marks in each panel show the maximum and minimum values for each property, respectively. The results are related to the stiffness tensor calculated (a) at the B3LYP-D3 and (b) at the PBE-D2 levels of theory.

The percentage anisotropy (A%) of seismic velocities is defined in the present work as $A = 200(V_{max} - V_{min})/(V_{max} + V_{min})$, with V_{max} and V_{min} the maximum and minimum acoustic velocity found by exploring a hemisphere of all possible propagation directions. It is worth remembering that in anisotropic crystals, such as aragonite, there are two orthogonally polarized secondary waves, a fast one (V_{S1}) and a slow one (V_{S2}), for each propagation direction. As a consequence, the percentage anisotropy can be calculated for each direction V_{S1} and V_{S2}. The bidimensional projections reported in Figure 4 show that V_P waves travel faster along the [100] crystallographic direction and slower in the [001] direction, with an anisotropy of 29.3% for PBE-D2, 28.3% for B3LYP-D* and 28.8% for B3LYP-D3 simulations. As expected, the Neumann's principle, which states that any physical property of a crystal must be invariant with respect to its symmetry elements, is respected.

The percentage of S-wave anisotropy, also known as shear wave splitting, is about 30% for the PBE-D2 and B3LYP-D3 approaches, whereas it was larger (37%) at the B3LYP-D* level. These seismic wave anisotropies are in line with the previous theoretical observations of Huang and co-workers (2017), who obtained for the longitudinal waves $A(V_P)$ = 26% and for the transverse seismic waves $A(V_S)$ = 38%, calculated at 0 GPa.

The anisotropy of V_P/V_{S1} ratio is almost the same between the PBE-D2 (42.7%) and the B3LYP-D* (42.5%) levels of theory, but the V_P/V_{S2} ratio is about 10% different between the two approaches (52.3% with PBE-D2 and 62.6% with B3LYP-D*). This is obviously due to the values of the primary and secondary acoustic wave velocities obtained from the two simulations, which were calculated from slightly different stiffness tensors. By using the B3LYP-D3 approach, the ratios are close to the PBE-D2 ones.

Finally, no significant differences in the directions of maximum and minimum seismic velocities (black and white markers in Figure 4, respectively) were observed when the DFT Hamiltonian is changed. To our knowledge, this is the first time that a direct analysis of the effects of two density functionals and different DFT-D*n* schemes was performed on the elasticity of aragonite and on its seismic wave propagation.

Conclusions

In the present work, we provided a first-principle simulation to obtain a detailed analysis of the elastic properties of aragonite ($CaCO_3$, space group *Pmcn*), an important mineral polymorph in both geological and biological fields. We employed two well-known Density Functional Theory Hamiltonians, namely PBE and B3LYP, which were corrected with the DFT-D2 and DFT-D3 schemes to properly treat long-range interactions. Compared to previous simulations with the same approach (Gaussian-type orbitals basis sets and the hybrid B3LYP functional), the weak van der Waals interactions gave an important contribution to both the crystallographic and elastic properties of the mineral, in agreement with recent simulations carried out on

calcite, the low-pressure polymorph of calcium carbonate. The structural results suggest that the less empirical DFT-D3 approach should be preferred to treat this high-pressure phase, as it provides results that are more in line with the expected physical behaviour of aragonite, also compared to experimental data.

A new set of data at absolute zero (0 K) in both hydrostatic compression/expansion regimes was obtained from theoretical simulations up to about 25 GPa, which is below the known phase transition of aragonite to the post-aragonite phase. The energy versus unit cell volume results were fitted to a volume-integrated third-order Birch-Murnaghan equation of state, whose parameters are in line with recent experimental findings. From the analysis of the variation of the lattice parameters and internal geometry (bond lengths and angles, and CO_3^{2-} aplanarity) as a function of pressure, a possible suggestion of the beginning of a phase transition was observed by the stiffening of the **b**-axis values above about 15 GPa and by the decreasing of the aplanarity of the carbonate ion groups. To fully support this observation, further simulations at higher pressures on the post-aragonite structure are needed to investigate this issue at atomic level, obtaining the enthalpy variation at 0 K. However, for a complete thermodynamic assessment of this phase transition, temperature effects must be included, *e.g.*, using quasi-harmonic approximation or *ab initio* molecular dynamics simulations. The calculation of the lattice dynamics is a very demanding task from the computational side and a careful evaluation of the convergence on the thermodynamic results on the supercell size (at least a 2×2×2 supercell with 160 atoms should be considered) must be performed to obtain accurate data. This kind of analysis would also allow a better comparison between the experimental results at ambient conditions (1 atm, 298 K) and the theoretical simulations. We are currently working on this topic, which will be the subject of a future work.

In addition, we provided the second-order elastic moduli of orthorhombic aragonite at 0 GPa, whose values are in good agreement with previous theoretical and experimental ones. A set of mechanical properties was further derived from the stiffness matrix, which could be useful for material science applications. We also calculated the acoustic wave velocities of the mineral, which are very important from the geophysical perspective because they can be used to get information on the structure of the lower mantle of Earth.

Acknowledgements

The present work did not receive any specific funding. The authors wish to thank the University of Bologna supporting the present research.

Author Contributions

Conceptualization, G.U. and G.V.; methodology, G.U.; validation, G.U. and G.V.; formal analysis, G.U.; investigation, G.U. and G.V.; data curation, G.U.; writing—review and editing, G.U. and G.V.; visualization, G.U.; supervision, G.V. All authors have read and agreed to the published version of the manuscript.

Data availability

The data are available within the present paper.

References

Antao, S.M., and Hassan, I. (2009) The orthorhombic structure of $CaCO_3$, $SrCO_3$, $PbCO_3$ and $BaCO_3$: linear structural trends. Canadian Mineralogist, 47(5), 1245-1255.

Becke, A.D. (1993) A New Mixing of Hartree-Fock and Local Density-Functional Theories. Journal of Chemical Physics, 98(2), 1372-1377.

Becke, A.D., and Johnson, E.R. (2005) A density-functional model of the dispersion interaction. Journal of Chemical Physics, 123(15), 154101.

Birch, F. (1947) Finite elastic strain of cubic crystal. Physical Review, 71, 809-824.

Bragg, W.L. (1924) The structure of aragonite. Proceedings of the Royal Society A, 105(729), 16-39.

Broyden, C.G. (1970a) The convergence of a class of double-rank minimization algorithms: 1. General considerations. IMA Journal of Applied Mathematics, 6(1), 76-90.

-. (1970b) The convergence of a class of double-rank minimization algorithms: 2. The new algorithm. IMA Journal of Applied Mathematics, 6(3), 222-231.

Carteret, C., De La Pierre, M., Dossot, M., Pascale, F., Erba, A., and Dovesi, R. (2013) The vibrational spectrum of CaCO3 aragonite: A combined experimental and quantum-mechanical investigation. Journal of Chemical Physics, 138(1), 014201, 014201.

Caspi, E.N., Pokroy, B., Lee, P.L., Quintana, J.P., and Zolotoyabko, E. (2005) On the structure of aragonite. Acta Crystallographica Section B: Structural Science, 61(2), 129-132.

Civalleri, B., Zicovich-Wilson, C.M., Valenzano, L., and Ugliengo, P. (2008) B3LYP augmented with an empirical dispersion term (B3LYP-D*) as applied to molecular crystals. CrystEngComm, 10(4), 405-410.

Dasgupta, R., and Hirschmann, M.M. (2010) The deep carbon cycle and melting in Earth's interior. Earth and Planetary Science Letters, 298(1-2), 1-13.

De Villiers, J.P.R. (1971) Crystal structures of aragonite, strontianite and witherite. American Mineralogist, 56(758-767), 11.

Dovesi, R., Erba, A., Orlando, R., Zicovich-Wilson, C.M., Civalleri, B., Maschio, L., Rerat, M., Casassa, S., Baima, J., Salustro, S., and Kirtman, B. (2018) Quantum-mechanical condensed matter simulations with CRYSTAL. Wiley Interdisciplinary Reviews-Computational Molecular Science, 8(4), E1360.

Erba, A., Mahmoud, A., Belmonte, D., and Dovesi, R. (2014) High pressure elastic properties of minerals from ab initio simulations: The case of pyrope, grossular and andradite silicate garnets. Journal of Chemical Physics, 140(12), 124703.

Farfan, G.A., Apprill, A., Cohen, A., DeCarlo, T.M., Post, J.E., Waller, R.G., and Hansel, C.M. (2021) Crystallographic and chemical signatures in coral skeletal aragonite. Coral Reefs, 41, 19-34.

Fisler, D.K., Gale, J.D., and Cygan, R.T. (2000) A shell model for the simulation of rhombohedral carbonate minerals and their point defects. American Mineralogist, 85(1), 217-224.

Fletcher, R. (1970) A new approach to variable metric algorithms. The Computer Journal, 13(3), 317-322.

Gaillac, R., Pullumbi, P., and Coudert, F.X. (2016) ELATE: an open-source online application for analysis and visualization of elastic tensors. Journal of Physics-Condensed Matter, 28(27), 275201.

Goldfarb, D. (1970) A family of variable-metric methods derived by variational means. Mathematics of Computation, 24, 23-26.

Grimme, S. (2006) Semiempirical GGA-type density functional constructed with a long-range dispersion correction. Journal of Computational Chemistry, 27(15), 1787-1799.

Grimme, S., Antony, J., Ehrlich, S., and Krieg, H. (2010) A consistent and accurate ab initio parametrization of density functional dispersion correction (DFT-D) for the 94 elements H-Pu. Journal of Chemical Physics, 132(15), 154104.

Hebbache, M., and Zemzemi, M. (2004) Ab initio study of high-pressure behavior of a low compressibility metal and a hard material: Osmium and diamond. Physical Review B, 70(22), 224107.

Huang, D., Liu, H., Hou, M.Q., Xie, M.Y., Lu, Y.F., Liu, L., Yi, L., Cui, Y.J., Li, Y., Deng, L.W., and Du, J.G. (2017) Elastic properties of CaCO3 high pressure phases from first principles. Chinese Physics B, 26(8), 089101.

Johannes, W., and Puhan, D. (1971) The calcite-aragonite transition, reinvestigated. Contributions to Mineralogy and Petrology, 31(1), 28-38.

Johnson, E.R., and Becke, A.D. (2005) A post-Hartree-Fock model of intermolecular interactions. Journal of Chemical Physics, 123(2), 024101.

-. (2006) A post-Hartree-Fock model of intermolecular interactions: Inclusion of higher-order corrections. Journal of Chemical Physics, 124(17), 174104.

Lee, C.T., Yang, W.T., and Parr, R.G. (1988) Development of the Colle-Salvetti Correlation-Energy Formula into a Functional of the Electron-Density. Physical Review B, 37(2), 785-789.

Li, Y., Zou, Y., Chen, T., Wang, X., Qi, X., Chen, H., Du, J., and Li, B. (2015) P-V-T equation of state and high-pressure behavior of CaCO3 aragonite. American Mineralogist, 100(10), 2323-2329.

Litasov, K.D., Shatskiy, A., Gavryushkin, P.N., Bekhtenova, A.E., Dorogokupets, P.I., Danilov, B.S., Higo, Y., Akilbekov, A.T., and Inerbaev, T.M. (2017) P-V-T equation of state of CaCO3 aragonite to 29 GPa and 1673 K: In situ X-ray diffraction study. Physics of the Earth and Planetary Interiors, 265, 82-91.

Liu, L.G., Chen, C.C., Lin, C.C., and Yang, Y.J. (2005) Elasticity of single-crystal aragonite by Brillouin spectroscopy. Physics and Chemistry of Minerals, 32(2), 97-102.

Mainprice, D., Hielscher, R., and Schaeben, H. (2011) Calculating anisotropic physical properties from texture data using the MTEX open-source package. Geological Society Special Publication, 360, p. 175-192.

Marmier, A., Lethbridge, Z.A.D., Walton, R.I., Smith, C.W., Parker, S.C., and Evans, K.E. (2010) ElAM: A computer program for the analysis and representation of anisotropic elastic properties. Computer Physics Communications, 181(12), 2102-2115.

Martinez, I., Zhang, J., and Reeder, R.J. (1996) In situ X-ray diffraction of aragonite and dolomite at high pressure and high temperature: Evidence for dolomite breakdown to aragonite and magnesite. American Mineralogist, 81(5-6), 611-624.

Momma, K., and Izumi, F. (2008) VESTA: a three-dimensional visualization system for electronic and structural analysis. Journal of Applied Crystallography, 41, 653-658.

Monkhorst, H.J., and Pack, J.D. (1976) Special points for Brillouin-zone integrations. Physical Review B, 8, 5188-5192.

Mouhat, F., and Coudert, F.X. (2014) Necessary and sufficient elastic stability conditions in various crystal systems. Physical Review B, 90(22), 224104.

Musgrave, M.J.P. (1970) Crystal Acoustics: introduction to the study of elastic waves and vibrations in crystals. Holden-Day, San Francisco, CA, USA.

Nye, J.F. (1957) Physical properties of crystals. Oxford University Press, Oxford.

Oganov, A.R., Glass, C.W., and Ono, S. (2006) High-pressure phases of $CaCO_3$: crystal structure prediction and experiment. Earth and Planetary Science Letters, 241(1-2), 95-103.

Ono, S., Kikegawa, T., and Ohishi, Y. (2007) High-pressure transition of CaCO3. American Mineralogist, 92(7), 1246-1249.

Ono, S., Kikegawa, T., Ohishi, Y., and Tsuchiya, J. (2005) Post-aragonite phase transformation in CaCO3 at 40 GPa. American Mineralogist, 90(4), 667-671.

Ottonello, G., Civalleri, B., Ganguly, J., Perger, W.F., Belmonte, D., and Zuccolini, M.V. (2010) Thermo-chemical and thermo-physical properties of the high-pressure phase anhydrous B ($Mg_{14}Si_5O_{24}$): An ab-initio all-electron investigation. American Mineralogist, 95(4), 563-573.

Palaich, S.E.M., Heffern, R.A., Hanfland, M., Lausi, A., Kavner, A., Manning, C.E., and Merlini, M. (2016) High-pressure compressibility and thermal expansion of aragonite. American Mineralogist, 101(7), 1651-1658.

Pavese, A., Catti, M., Price, G.D., and Jackson, R.A. (1992) Interatomic potentials for $CaCO_3$ polymorphs (calcite and aragonite), fitted to elastic and vibrational data. Physics and Chemistry of Minerals, 19(2), 80-87.

Perdew, J.P., Burke, K., and Ernzerhof, M. (1996) Generalized gradient approximation made simple. Physical Review Letters, 77(18), 3865-3868.

Perger, W.F., Criswell, J., Civalleri, B., and Dovesi, R. (2009) Ab-initio calculation of elastic constants of crystalline systems with the CRYSTAL code. Computer Physics Communications, 180(10), 1753-1759.
Plank, T., and Langmuir, C.H. (1998) The chemical composition of subducting sediment and its consequences for the crust and mantle. Chemical Geology, 145(3-4), 325-394.
Salje, E., and Viswanathan, K. (1976) The phase diagram calcite-aragonite as derived from the crystallographic properties. Contributions to Mineralogy and Petrology, 55(1), 55-67.
Santillán, J., and Williams, Q. (2004) A high pressure X-ray diffraction study of aragonite and the post-aragonite phase transition in CaCO3. American Mineralogist, 89(8-9), 1348-1352.
Shanno, D.F. (1970) Conditioning of quasi-Newton methods for function minimization. Mathematics of Computation, 24, 647-656.
Ulian, G., Moro, D., and Valdrè, G. (2018) First principle investigation of the mechanical properties of natural layered nanocomposite: Clinochlore as a model system for heterodesmic structures. Composite Structures, 202, 551-558.
-. (2021a) Benchmarking dispersion-corrected DFT methods for the evaluation of materials with anisotropic properties: Structural, electronic, dielectric, optical and vibrational analysis of calcite ($CaCO_3$, space group: R-3c). Physical Chemistry Chemical Physics, 23(34), 18899-18907.
Ulian, G., Moro, D., and Valdrè, G. (2021b) Elastic properties of heterodesmic composite structures: The case of calcite CaCO3 (space group $R\bar{3}c$). Composites Part C: Open Access, 6, 100184.
Ulian, G., and Valdrè, G. (2017) Effects of fluorine content on the elastic behavior of topaz Al2SiO4(F,OH)(2). American Mineralogist, 102(1-2), 347-356.
-. (2018a) Equation of state of hexagonal hydroxylapatite (P6(3)) as obtained from density functional theory simulations. International Journal of Quantum Chemistry, 118(12), e25553, e25553.
-. (2018b) Second-order elastic constants of hexagonal hydroxylapatite ($P6_3$) from ab initio quantum mechanics: comparison between DFT functionals and basis sets. International Journal of Quantum Chemistry, 118(5), e25500, e25500.
-. (2022a) QUANTAS, a Python software for the analysis of solids from ab initio quantum mechanical simulations and experimental data. Journal of Applied Crystallography, 55(2), 386-396.
-. (2022b) Study of the variation of the optical properties of calcite with applied stress, useful for specific rock and material mechanics. Scientific Reports, 12(1), 299, 299.
Ungureanu, C.G., Prencipe, M., and Cossio, R. (2010) Ab initio quantum-mechanical calculation of $CaCO_3$ aragonite at high pressure: thermodynamic properties and comparison with experimental data. European Journal of Mineralogy, 22(5), 693-701.
Valenzano, L., Torres, F.J., Klaus, D., Pascale, F., Zicovich-Wilson, C.M., and Dovesi, R. (2006) Ab initio study of the vibrational spectrum and related properties of crystalline compounds; the case of $CaCO_3$ calcite. Zeitschrift Fur Physikalische Chemie-International Journal of Research in Physical Chemistry & Chemical Physics, 220(7), 893-912.
Vizgirda, J., and Ahrens, T.J. (1982) Shock compression of aragonite and implications for the equation of state of carbonates. Journal of Geophysical Research, 87(B6), 4747-4758.
Voigt, W. (1910) Lehrbuch der Kristallphysik. Teubner, Leipzig, Germany.
Wang, M., Liu, Q., Nie, S., Li, B., Wu, Y., Gao, J., Wei, X., and Wu, X. (2015) High-pressure phase transitions and compressibilities of aragonite-structure carbonates: SrCO3 and BaCO3. Physics and Chemistry of Minerals, 42(6), 517-527.